Plasticity induced heating in the fracture and cutting of metals

Alan T. Zehnder, Yogesh K. Potdar & Kavi Bhalla
Department of Theoretical and Applied Mechanics
Cornell University, Ithaca, NY, USA.

Abstract

During high speed deformation of metals, dissipation of inelastic work and frictional heating can result in significant temperature increase in the material being deformed. Temperature increase can strongly modify the deformation deformation process via thermal softening of the material. If the temperature field can be accurately measured, via thermal imaging for example, then the temperature rise can be used to probe both the deformation process and the state of the material undergoing deformation or failure. As temperature rise stems principally from thermal dissipation of plastic work, experiments and theories on the fraction of plastic work dissipated thermally are summarized and discussed. Large temperature increases can occur during dynamic crack growth in ductile materials. The temperature rise at the tip of dynamically propagating cracks is measured experimentally and the impact of temperature rise on dynamic fracture toughness is studied via a partially coupled thermomechanical analysis. During stable crack tearing, although the temperature rise may be small, thermal images of temperature rise can be used to quantify energy flux to the crack, leading to potential applications of thermal imaging in destructive testing of energy absorbing structures. In addition to heating by plastic work, frictional heating contributes significantly to temperature rise during metal cutting. High temperatures in cutting may be beneficial, leading to lower cutting forces, or may be detrimental, leading to reduced cutting tool life. Experiments are performed to measure temperature increases on the very fast time scales and small size scales associated with deformation and failure of metals during orthogonal cutting.

1 Introduction

It has long been known that the work of plastic deformation in metals is largely dissipated as thermal energy with the balance stored in the material as defect energy and as residual strain energy due to incompatible slip. It is said that Tresca (ca. 1870) was the first to notice and record heating due to plastic deformation, Bell [1]. However, the modern study of thermomechanics originated with the work of Taylor, Farren and Quinney [2, 3], who in 1925 and 1934 published measurements of thermal energy dissipated during the plastic deformation of various metals. Since then many further experiments have been performed, Bever et al. [4], mostly from the perspective of materials scientists interested not in the energy dissipated, but in the energy stored and its effects on recrystallization. In fracture initiation, rapid crack growth, metal cutting and other high

speed deformation processes involving material separation, interest in the dissipation of energy is due to the heating produced and due to the effect of heating on the process. Temperature increase in such deformations leads to thermal softening of the material, promoting further deformation and more heating. The temperature rise, if it can be accurately measured, can be used experimentally to probe the deformation process, allowing one, for example, to determine local rates of energy dissipation in a structure. In manufacturing processes, such as metal cutting, heating due to plastic work and due to friction can lead to high temperatures which are detrimental to cutting tool life. Thermal softening in cutting may also lead to segmented and discontinuous chip formation, which affects many aspects of cutting, including cutting system vibrations, surface finish, and chip formation.

Elements of thermomechanical coupling theory are reviewed in section 2. The conversion of plastic work to thermal energy is reviewed in section 3. Section 4 looks at measurement the increase in temperature during dynamic crack growth and at the effect of temperature rise on the fracture process. Recent work using thermal images to quantify energy flux to the crack tip during stable crack tearing is presented in section 5. Measurements and analysis of temperature in metal cutting, a process similar to crack tearing, are discussed in section 6.

2 Theory of thermomechanical coupling in solids

Temperature, heat flow, material properties, stress and deformation all depend on each other, and hence are said to be coupled. This coupling often goes unnoticed, since many problems involve either slow loading, where thermal energy can be dissipated to the environment with little temperature increase, or the problems involve elastic deformations, where temperature changes are small, on the order of 1°C. However, when the deformation involves significant plastic flow over a time scale too short for thermal energy to be dissipated, thermomechanical coupling becomes a significant factor in the problem.

The fundamental thermomechanical equations for solids are reviewed in simple form here. A more complete discussion of thermomechanics theory is given in Maugin [5]. The theory of thermoelasticity is given by Carlson [6]. For homogeneous, isotropic materials, assuming classical plasticity, the relevant solid mechanics field equations are:

$$\dot{\epsilon}_{ij} = \frac{1}{2}(\dot{u}_{i,j} + \dot{u}_{j,i}), \tag{1}$$

$$\sigma_{ij,j} + b_i = \rho \ddot{u}_i, \tag{2}$$

$$\dot{\epsilon}_{ij} = \dot{\epsilon}^e_{ij} + \dot{\epsilon}^T_{ij} + \dot{\epsilon}^p_{ij}, \tag{3}$$

$$\dot{\epsilon}^e_{ij} = \frac{1}{2\mu}\left(\dot{\sigma}_{ij} - \frac{\lambda}{3\lambda + 2\mu}\dot{\sigma}_{kk}\delta_{ij}\right), \tag{4}$$

$$\dot{\epsilon}^T_{ij} = \alpha \dot{T}\delta_{ij}, \tag{5}$$

$$\dot{\epsilon}^p_{ij} = g(\sigma_{eq}, T, \kappa)\frac{S_{ij}}{\sigma_{eq}}, \tag{6}$$

where κ is an internal variable that evolves as

$$\dot{\kappa} = h(\sigma_{eq}, T, \kappa)\dot{\epsilon}_{eq}, \tag{7}$$

$\dot{\epsilon}_{ij}$ are components of the strain rate tensor, $\dot{u}_i$ are velocity components, σ_{ij} is the stress tensor, b_i are body force components, ρ is the density, λ and μ are the Lamé elastic constants, α is the coefficient of thermal expansion, T is temperature, S_{ij} is the deviatoric stress, $\sigma_{eq} \equiv (\frac{3}{2}S_{ij}S_{ij})^{1/2}$, and $\epsilon_{eq} \equiv (\frac{2}{3}\epsilon_{ij}\epsilon_{ij})^{1/2}$. In all of the above, the material constants generally vary with temperature.

The heat conduction equation with mechanical coupling is

$$(kT_{,i})_{,i} - \alpha(3\lambda + 2\mu)T_0\dot{\epsilon}_{kk} + \beta\sigma_{ij}\dot{\epsilon}^p_{ij} = \rho c\dot{T}, \tag{8}$$

where k is the thermal conductivity, T_0 is the ambient temperature (in absolute temperature units), c is the specific heat, and β is the fraction of plastic work dissipated thermally. In general

$$\beta = \beta(\epsilon^p_{eq}, \dot{\epsilon}^p_{eq}, T). \tag{9}$$

Thermal conductivity, density and specific heat vary with temperature. The second term in eq. (8) represents the thermoelastic cooling that occurs during the adiabatic expansion of a solid. The third term of eq. (8) represents the dissipation of plastic work as thermal energy - the primary focus of this work.

Thermomechanical coupling is seen in the temperature dependence of plastic strain rate, temperature dependence of elastic and thermal constants, the presence of thermal strain, heat generated by plastic flow, and the thermoelastic term in eq. (8). When plastic deformation is present, thermal expansion, eq. (5) and thermoelastic effects, eq. (8) are small in proportion to other terms and can often be neglected. For example, for 1018 CRS, a deformation with $\epsilon^p = 1$, yields $\Delta T \approx 130°C$. A temperature rise of 130°C in 1018 CRS reduces the elastic modulus by 30%, and the yield stress by 6%. When there is no plastic deformation, there is only thermoelastic heating or cooling. For 1018 CRS under uniaxial tension, the thermoelastic cooling will be $\Delta T = -.46°C$ just before yield.

If an initially hot object with characteristic dimension l and thermal diffusivity $a \equiv k/\rho c$ is cooled on its surface at time $t = 0$, the rate of cooling scales with the Fourier number $Fo \equiv at/l^2$. When $Fo \ll 1$, heat loss is negligible, and process can be considered to be adiabatic. When $Fo \gg 1$ the process is essentially isothermal. Consider, for example, a 10mm thick sample of steel. In this case $Fo = 1$ for $t = 7$s. Taking $\frac{1}{100}$ to be $\ll 1$ and 100 to be $\gg 1$, if a uniform deformation were to occur in $t < 0.07$s the process would be approximately adiabatic, while if the process occurred in $t > 700$s it would be approximately isothermal.

3 Thermal dissipation of plastic work

To perform simulations of thermomechanically coupled problems it is important to know what fraction of the plastic work remains as latent energy in the material, and what fraction is dissipated thermally. Let us define the fraction of plastic work dissipated thermally to be β,

$$\beta \equiv \frac{\dot{Q}^p}{\dot{W}^p} = 1 - \frac{\dot{Q}^s}{\dot{W}^p} \tag{10}$$

where $\dot{W}^p = \sigma_{ij}\dot{\epsilon}^p_{ij}$ is the plastic work rate, $\dot{Q}^p$ is the rate of thermal dissipation of plastic energy, and $\dot{Q}^s$ is the rate of energy storage. Although there are a great deal of experimental results on β, it is not yet possible to predict β based on theory.

3.1 Experimental measurements

As discussed by Bever et al. [4] measurements of β can be classified into two methods, (1) single step methods where plastic work and thermal dissipation are measured during or immediately after deformation, and (2) two-step methods where the stored energy is measured after deformation and after the sample has cooled.

In the single step methods the sample is deformed and the rate of or total plastic work is measured based on the applied loads and resulting deformation histories. The resulting temperature rise of the sample is measured continuously during the experiment, using thermocouples in contact with the test specimen, e.g. Taylor and Quinney[3] or by infrared thermometry, e.g. Hodowany et al. [7]. Such experiments are typically performed quickly so that $Fo \ll 1$ and the heating is adiabatic. In this adiabatic case β can be found from the measured stress, strain rate and temperature rise from eq. (8) with the conduction term $(kT,_i),_i$ neglected. However, Zehnder et al. [8] have recently demonstrated that with careful attention to analyzing heat losses, β can be measured in non-adiabatic experiments as well. A variation of the above method is to rapidly deform the sample, then quickly drop it into a calorimeter to measure the temperature rise and hence infer the total plastic dissipation energy, e.g. [3]. Adiabatic conditions are preferred for this variation. A third variation is to perform the experiment isothermally inside a calorimeter. For example, Williams [9] continuously measured $\dot{Q}^p$ by measuring the volume of CCl_3F evaporated by the heat of the test sample.

While most of the experimental data are for low strain rate deformations, in recent work by Mason et al. [10] and Hodowany et al. [7] a Kolsky bar was used to measure β at strain rates on the order of 1000/s. In these experiments the duration of the experiment is under 1 ms and the process is truly adiabatic. Temperature rise is measured using high speed IR detectors. Their method remains the only demonstrated approach capable of directly measuring β at high strain rates.

In the two step methods the sample is first deformed and the load-displacement curve recorded for the purposes of calculating the total plastic work applied, W^p. The stored energy, Q^s, is determined by annealing the sample and measuring the difference in energy released by the sample relative to that released by an undeformed sample of the same material. As Bever et al. [4] discuss there are a large number of variations of this method, including using isothermal annealing, anisothermal annealing and reaction methods.

Of the great many experimental measurements of β, or of $\dot{Q}^s/\dot{W}^p$ a few are summarized in Figure 1. Additional data on β are reviewed by MacDougall [12]. Several general trends can be observed from these data. In all of the metals β approaches 0.9 to 1.0 for large strain. At low strains several of the results show β initially decreasing, then increasing beyond strains of 20% or so. The little data available for the variation of β with strain rate show that for materials whose initial flow stress increases with strain rate, β increases with strain rate as well. An example is shown in the α Ti data shown in Figure 1. The very low value of β at low strain rates for Al 2024 are surprising. A different aluminum, Al BS 2011, also shows very low initial β, however it increases rapidly with strain. Nonetheless, even for Al 2024, β eventually approaches a value close to one. Results of recent experiments by Kapoor and Nemat-Nasser [13], where flow stress is cleverly used as a probe of temperature, argue strongly for β values approaching one for large strains, consistent with most of the data presented in Figure 1.

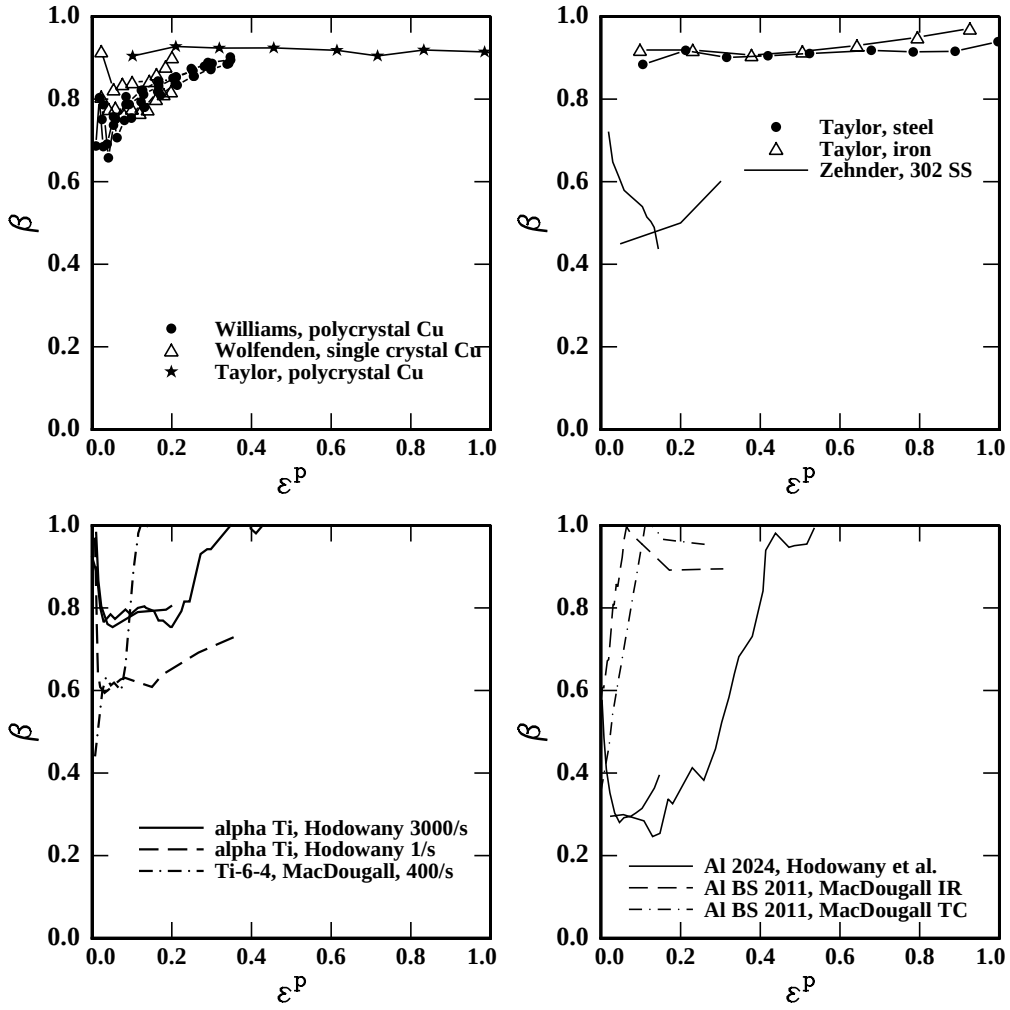

Figure 1: β versus ϵ^p for several metals. Copper data from Williams [9], Wolfenden [11] and Taylor and Quinney [3]. Steel and iron data from Taylor and Quinney [3]. 302 SS data from Zehnder, et al. [8] and new results. α Ti and Al 2024 data from Hodowany et al. represent the approximate average of their results [7]. MacDougall's [12] Al. results obtained using infrared radiometry (IR) and thermocouples (TC) to measure temperature rise. Ti-6Al-4V results from MacDougall [12].

3.2 Theory

A simple theory for predicting β is based on assuming that the stored energy of cold work is in the form of dislocation line energy, Nabarro [14], Zehnder [15]. By developing expressions relating dislocation density (and hence stored energy density) to flow stress, such models predict

$$\beta \sim 1 - C \frac{1}{E} \frac{\partial \sigma_{eq}}{\partial \epsilon^p_{eq}}, \tag{11}$$

where C is a constant that in principle could be determined by detailed analysis of dislocation configuration, $\partial \sigma_{eq} / \partial \epsilon^p_{eq}$ is the tangent modulus (slope of the plastic stress-strain curve) and E is the elastic modulus. These models predict that when hardening is high β is low, and when the material stops hardening $\beta \to 1$. In most metals hardening is highest at the start of plastic deformation, thus this model predicts a continuously increasing β. This prediction is consistent with many, but not all experimental data. For example, the values of β for Cu can be well approximated by the above expression, as can the β for Al BS 2011. However, Al 2024 behaves much differently. In this material, although there is very little hardening, β is small until strains reach approximately 30%.

Aravas et al. [16] developed a theory for the stored energy of cold work, based on residual elastic strains due to incompatible slip in a polycrystalline material consisting of of elastic-perfectly plastic crystals. The theory provides an estimate for Q^s/W^p, and hence for β. In rough accord with dislocation based theories, Aravas's theory predicts higher β for materials with less work hardening. This theory also predicts that when hardening stops, storage of cold work stops and hence $\beta \to 1$. This theory predicts that for low strains β is a decreasing function of strain, consistent with results for Al 2024, 302 SS, Ti and perhaps Cu at low strains.

A recent theory by Rosakis et al. [17] proves that the stored energy of cold work cannot depend on rate. Using this result one can predict how the dissipated energy will vary with strain rate if the rate dependent material properties are known. Thus this theory provides a powerful new tool for determining β at high strain rates without needing high speed temperature measurements. One needs to measure the stress-strain response over a range of strain rates, using a Kolsky bar for example, and β at one strain rate, which could be relatively low, meaning that temperature rise could be measured using a simple thermocouple. Then the theory can be used to predict β for the other strain rates.

4. Dynamic crack growth

When a crack grows at very high speeds the dissipated energy of plastic work results in a local temperature increase, that due to the high crack growth speed, cannot be conducted away from the crack tip prior to fracture. The crack tip temperature rise can be quite substantial, and hence can play an important role in determining dynamic fracture toughness of materials.

Early attempts at predicting the form of the temperature fields associated with crack growth made simplifying assumptions about the fracture process and the crack tip mechanical fields. Rice and Levy [18] used the Dugdale line concentrated yield zone model to calculate the plastic work rate near the tip of a running crack in ductile materials. Assuming complete conversion of plastic work to heat, they predicted the temperature rise by using the approach of Carslaw and Jaeger [19] to solve the heat equation as a

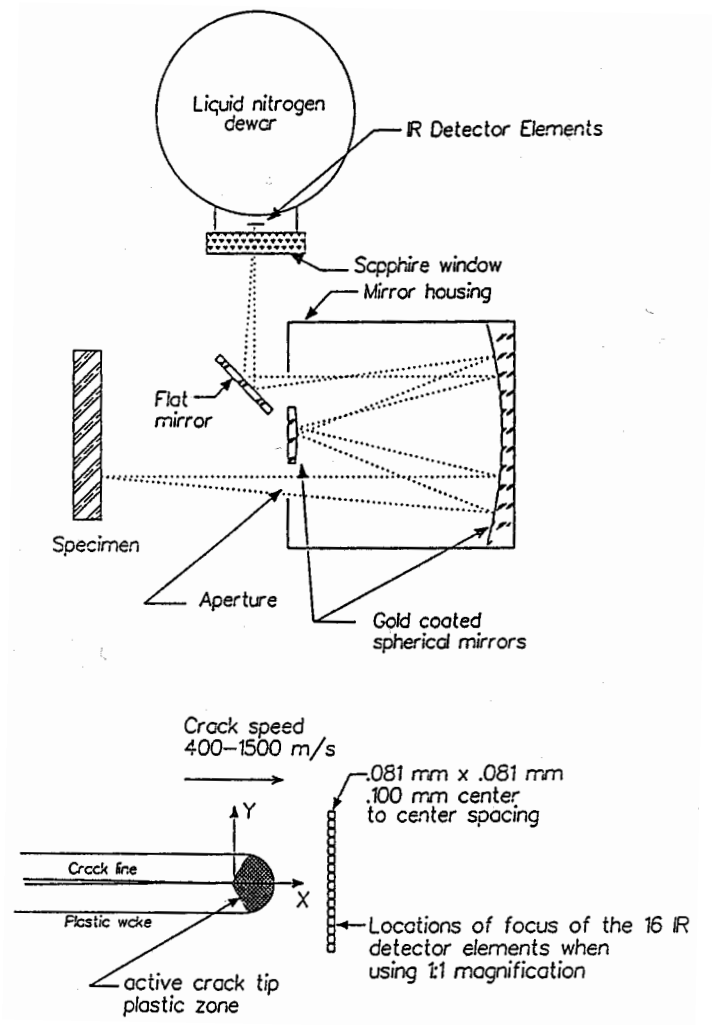

Figure 2: Experimental setup for measurement of temperature near the tip of dynamically propagating cracks. Radiation from the test specimen is focused onto the IR array using a 1:1 reflective lens system, from [28].

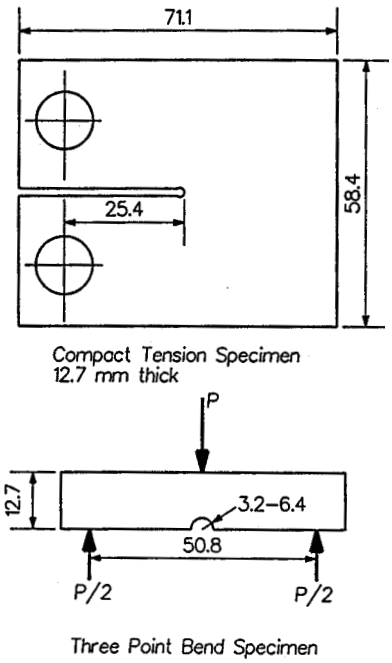

Figure 3: Test specimens for dynamic crack growth experiments with β-C titanium alloy, from [28].

superposition of a continuous distribution of point heat sources. In the absence of full field solutions for the stress and strain fields, other efforts assumed a form for the plastic zone. Weichert and Schönert [20, 21] calculated the temperature field for heat sources distributed uniformly in circular and rectangular plastic zones attached to a steadily growing crack. Kuang and Atluri [22] assumed a $1/r$ distribution of plastic work rate and computed the resulting temperature field by using a moving mesh finite element analysis (FEA). Bui, et al. [23] used the asymptotic mechanical fields for a growing crack in an elastic plastic solid to numerically study the resulting temperature field. They compare their results with infrared images of a slow moving crack.

Recent advances in computing have made it possible to compute the solution of problems that would be intractable analytically, such as, computation of the mechanical fields associated with crack growth in materials which have a general constitutive behavior. Malali [24] used FEA to compute the work rate field for a dynamic Mode III crack in an elastic-plastic material and then computed the temperature distribution as the solution to the superposition of distributed heat sources. Li et al. [25] numerically computed the shape and form of the plastic zone for varying crack speeds in a linear hardening elastic plastic solid in small scale yielding. They then obtained an Eulerian description of the thermal field for steady state crack growth using FEA.

Taken together, the estimates for peak crack tip temperature range from 2°C to 3000°C. To make sense of these competing estimates Zehnder and Rosakis [26, 27] developed a unique experimental setup to *directly* measure the temperature at the tip of dynamically propagating cracks. This system was further developed by Kallivayalil and

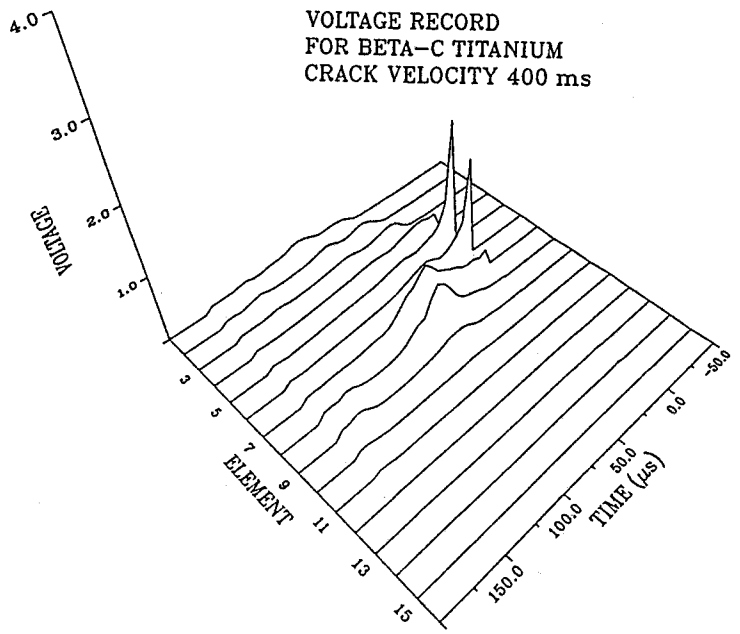

Figure 4: Voltage output from the 16 high speed IR detectors for a dynamic crack growth experiment with β-C Ti, from [28]

Zehnder [28].

Kallivayalil and Zehnder's experimental setup is shown schematically in Figure 2. Thermal radiation emitted by the sample due to crack tip heating is focused onto the infrared detectors using a 1:1 reflective imaging system. The detectors are a 16 element indium antimonide (InSb) linear array, each with its own amplifier. The IR elements are 81μm square with a center-to-center spacing of 100μm. During an experiment, outputs from all 16 detector elements are recorded simultaneously, at 10 MHz per channel, using 16 channels of high speed digitizers (Nicolet 4094 and Tektronix 390AD). As shown in Figure 2 the IR detectors focus on a line segment perpendicular to the path of the growing crack. As the crack runs past this segment, the temperature at these points is recorded. Crack position is measured using a conductive grid technique, thus the record of temperature vs. time at the 16 points can be converted into contours of temperature around the crack tip.

The experiments were performed using the high strength ($\sigma_0 = 1100$ MPa) titanium alloy β-C. Blunt notched compact tension and three point bend specimens, as shown in Figure 3 were statically loaded to fracture. Due to the initial notch bluntness, once the crack initiated it ran at very high speeds (up to 1000 m/s).

Figure 4 shows the raw data from each of the 16 IR detector elements for one experiment. The voltage was converted to temperature through the (non-linear) calibration of sample surface temperature and IR detector output. The time axis is converted into position by using the crack length record measured from the grid, and the resulting data used to plot contours of temperature rise around the crack tip in Figure 5. Note that

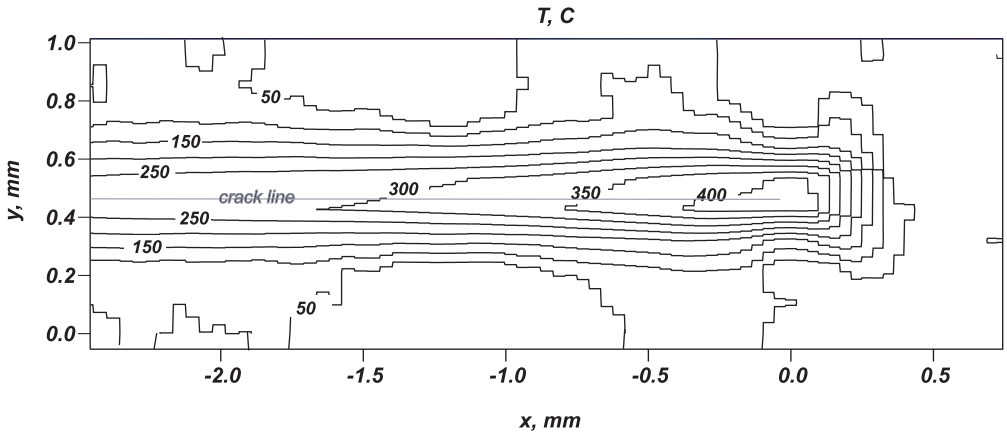

Figure 5: Crack tip temperature field for crack growing at 400 m/s in β-C titanium. Crack is moving from left to right in this picture. The peak crack tip temperature is over 400°C, after [28].

the peak crack tip temperature is over 400°C for this experiment. The contours of temperature extend essentially parallel to the crack line, showing that over the short time scale of dynamic crack growth, there is little time for heat conduction and the process is essentially adiabatic.

Such large temperature increases are enough to reduce the elastic modulus of β-C Ti by 25%, and the flow stress by 20% [29]. Beyond 400°C the flow stress drops even more rapidly. Thus the experimental data suggest that crack tip temperature rise may play a significant role in determining dynamic fracture toughness. To study the effect of temperature Kallivayalil, Hui and Zehnder [29] performed an analysis of crack growth with and without heating. This was a partially coupled analysis where the measured crack tip temperature fields were used to solve the problem of steady-state thermo-viscoplastic crack growth. The results of the analysis are summarized in Figure 6, which plots the calculated variation of dynamic fracture toughness with crack speed. Note that consistent with other viscoplastic models of crack growth, the curve is concave down. Two possible fracture criteria were considered. Brittle fracture was modeled by a critical stress criterion. Ductile fracture was modeled by a critical strain criterion. The analysis shows that for both the isothermal and thermal-effects cases a transition from ductile to brittle fracture can occur at high crack speeds. Accounting for thermal effects delays the onset of transition, increasing the fracture toughness of the material by about 20%.

5 Stable crack tearing

In contrast with dynamic crack growth, during stable crack tearing the heat generated has more time to diffuse away from the process zone and the resulting temperature field is generally not strong enough to significantly affect material properties such as flow stress and modulus of elasticity. However, we demonstrate here that even for slow moving cracks, where heat conduction plays an important role, the measured temperature field can be used to obtain quantitative information about the energy required to drive the crack and a qualitative description of the distributed damage to the material.

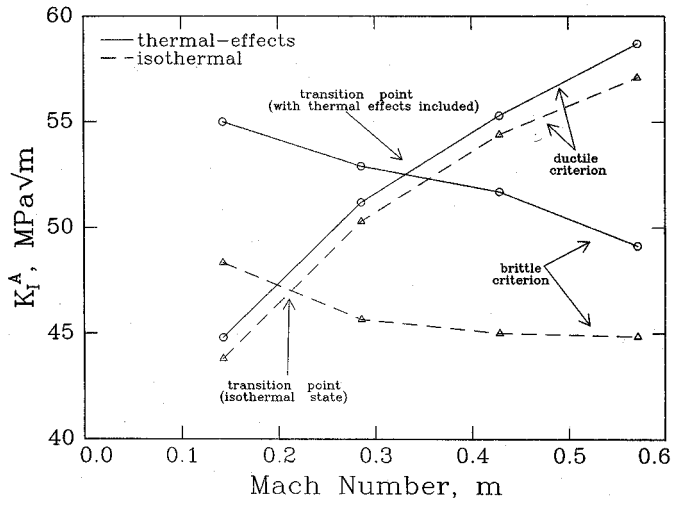

Figure 6: Dynamic fracture toughness versus normalized crack speed, m=v/c_s, where c_s is the shear wave speed, based on analysis of crack growth in β-C Ti. A temperature and rate dependent constitutive model is assumed. Shown are the toughnesses assuming either a brittle or a ductile fracture criterion. The results show that crack tip heating will delay the onset of ductile to brittle transition for materials subject to this phenomenon, from [29].

In our research, we have measured the temperature field ahead of a slow moving, mode I crack in 302 stainless steel (302 SS) using infrared imaging. These experiments were simulated using ABAQUS [30], a commercially available FEA code, to perform coupled thermal stress analysis of the transient heat conduction problem. Results from the FEA, such as the distribution of plastic work and the energy flux to the crack tip, are compared with those computed from the infrared images.

5.1 Theoretical background for analysis of thermal images

The thermal field is connected to the mechanical fields through β, the fraction of plastic work converted to heat. If the temperatures generated are not high enough to affect material properties, the thermal fields can be computed in a linear fashion by first solving the mechanical problem and then performing the thermal analysis. Otherwise temperature must be included as a field variable and a coupled thermomechanical problem solved.

Let us specialize the heat conduction equation (8) to a thin sheet in 2D plane stress conditions with no through thickness temperature gradients. Losses due to convection and radiation, which would appear as boundary conditions in eq. (8), can then be accounted for explicitly. If H_{loss} is this loss, per unit area, then

$$\beta\sigma_{ij}\dot{\epsilon_{ij}}^p + k\nabla^2 T - \alpha(3\lambda + 2\mu)T_0\dot{\epsilon}_{kk} - \frac{2}{l}H_{loss} = \rho c\dot{T}, \tag{12}$$

where l is the thickness of the sheet.

In comparison with the plastic-thermal dissipation occurring ahead of a growing crack in a ductile material, the effect of thermoelastic cooling is negligible. Losses due

to convection and radiation can be shown to be much smaller than the other terms for the problem considered in this study and have been ignored. Under these assumptions, the plastic work rate is obtained in terms of the temperature field,

$$\sigma_{ij}\dot{\epsilon_{ij}}^p = \frac{\rho c\dot{T} - k\nabla^2 T}{\beta}. \tag{13}$$

The energy required to drive the crack per unit crack advance, G, is closely related with the plastic work consumed in the process zone of the crack. Consider a coordinate system attached to the tip of the propagating crack. Let Γ be a contour, fixed in this coordinate system, that runs around the crack tip from one crack face to the other. Moran and Shih [31], starting from a general balance law, present a unified derivation for crack tip flux integrals. This can be specialized for flux of mechanical work through Γ as it is shrunk to the crack tip,

$$G_{tip} = \lim_{\Gamma \to 0} \frac{1}{v} \int_{\Gamma} [\sigma_{ij} n_i \frac{\partial u_i}{\partial t} + (U+T) v n_1] d\Gamma, \tag{14}$$

where v is crack speed, $\vec{n}$ is the unit normal vector directed outward from Γ and U and T are the stress work density and kinetic energy density, respectively. Freund [32] has shown that for quasistatic steady crack growth, (14) can be rewritten as

$$G_{tip} = G - \frac{1}{v} \int_{A_p} \sigma_{ij}\dot{\epsilon_{ij}}^p dA_p - \int_{-h}^{h} U_e^* dy, \tag{15}$$

where G is the energy provided by the remote loading, A_p is the active plastic zone, h is the thickness of the plastic wake behind the crack and U_e^* is the elastic strain energy locked in the wake due to the development of incompatible plastic strains. U_e^* is small when compared with the energy associated with plasticity and is ignored. Freund [32] further points out that for rate-independent plasticity $G_{tip} = 0$. Thus, energy flux to the crack is given by

$$G = \frac{1}{v} \int_{A_p} \sigma_{ij}\dot{\epsilon_{ij}}^p dA_p. \tag{16}$$

Substituting from (13), the energy flux to the crack can be written in terms of the temperature field as

$$G = \frac{1}{v\beta} \int_{A_p} (\rho c\dot{T} - k\nabla^2 T) dA_p. \tag{17}$$

This expression for G is inconvenient to work with since it requires computing the second spatial derivatives of the experimentally measured temperature field. It also involves the evaluation of the integral over a moving irregular shaped region. A series of modifications to (17) yields a form more suitable for evaluation from experimental data.

First, the divergence theorem is applied,

$$G = \frac{1}{v\beta} \left[\int_{A_p} \rho c\dot{T} dA_p - k \oint_{C_p} (T_x dy - T_y dx) \right], \tag{18}$$

where C_p is a contour that runs along the periphery of A_p. Finally, it is recognized that since plastic work is only associated with the process zone of the running crack, the

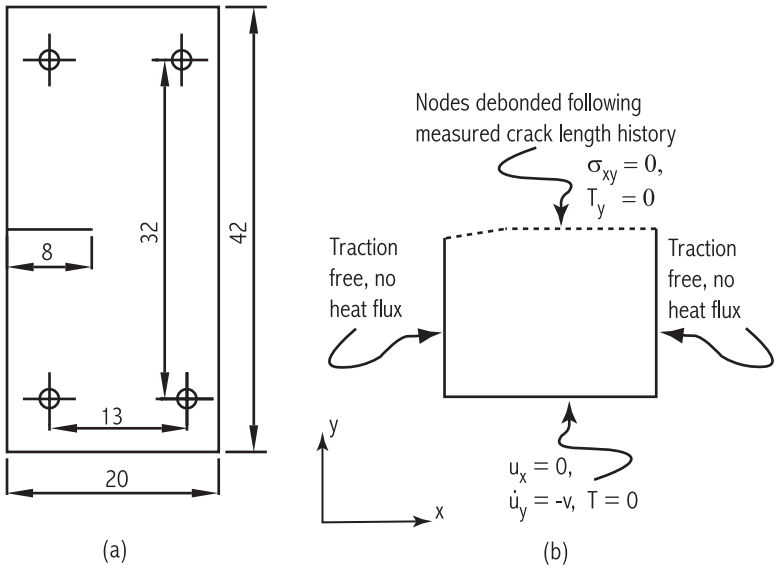

Figure 7: Single edge notched specimen (a) of vacuum annealed 302 stainless steel (0.1 mm thickness) and schematic of the symmetric half of specimen (b) used in FEA. Dimensions are in mm.

integral in (16) (and therefore (18)) remains unchanged as long as A_p encompasses the entire process zone. In fact, if we choose to work in a region large enough that there is no spatial temperature gradient across the boundary, the contour integral over C_p in (18) vanishes. Leaving,

$$G = \frac{1}{v\beta} \int_A \rho c \dot{T} dA, \tag{19}$$

where $A >> A_p$. In our analysis, the region of interest, A is the field of view of an infrared camera and is fixed in space. The flux of energy into and out of this region associated with material flowing through this spatially fixed boundary is considered negligible. We have computationally verified that this is a reasonable assumption if the region of interest is large enough.

Further simplifications result from recognizing that for a spatially fixed region the order of derivative and integral can be interchanged, so that,

$$G = \frac{1}{v\beta} \frac{d}{dt} \int_A \rho c T dA. \tag{20}$$

In the results presented here, G is computed using (18) and (19). We have verified, however, that the error associated with using (20) is negligible. The form of equation (20) makes several computational and experimental simplifications possible. The integral in (20) represents the total thermal energy of the material in the region, A. Thus, G, can be computed directly from the rate of change of total thermal energy in a region surrounding the crack. Thus, for instance, if the radiation from the entire region could be focused onto a single infrared detector, the energy flux to the crack could be computed.

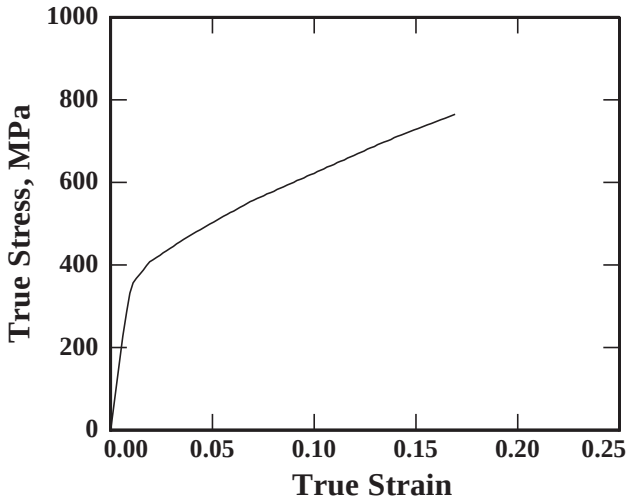

Figure 8: Evolution of flow stress from uniaxial test on 302 SS, from Zehnder, Babinsky and Palmer [8].

5.2 Experimental measurement of temperature field

The methodology described above was applied to carry out an analysis of the energy balance in mode I, plane stress crack growth in a ductile material. These experiments were performed at Wayne State University; the imaging system and its calibration are described in detail by Wang [33].

302 stainless steel (302 SS), obtained as shim stock, was restored to its virgin state by vacuum annealing. Single edge notched specimens, shown in Figure 7, were prepared. The use of thin specimens (0.1 mm thickness) ensured that surface temperatures were representative of through thickness temperature and conditions were close to plane stress. 302 SS is a good choice for material since it is ductile and strain hardens considerably, Figure 8, resulting in a large amount of plastic dissipation during crack growth. Compared with other steels, it also has low thermal conductivity. Prior research in our laboratory [8] has measured β, the fraction of plastic work converted to heat, for 302 SS as a function of strain at low strain rates, see Figure 1.

Specimens coated with a high emissivity black paint were mounted on a Rheometric Minimat tabletop tester and loaded in tension. A schematic of the experimental setup is shown in Figure 9. The load was measured using a 1000 N load cell and the analog signal was recorded on a Tektronix 2231 100 MHz digital oscilloscope. Tests were performed in displacement control using a constant cross head speed of 1.33 mm/s.

The failure process was imaged using an Amber/Raytheon Proview infrared imaging system. This IR camera consists of a focal plane array of 512x512 InSb detectors. The maximum framing rate and the maximum number of frames acquired in a test sequence are limited by a pixel digitization rate of 20 Million pixels/s and a data storage buffer of 32 Mbytes. For the results reported here, 256x256 of these detectors were focused on 24x24mm region, spanning the width of the specimen. 128 frames were acquired at a frame rate of 38.5 Hz resulting in a test duration of 3.32 seconds. The IR camera data acquisition was triggered by a signal from the Minimat tester.

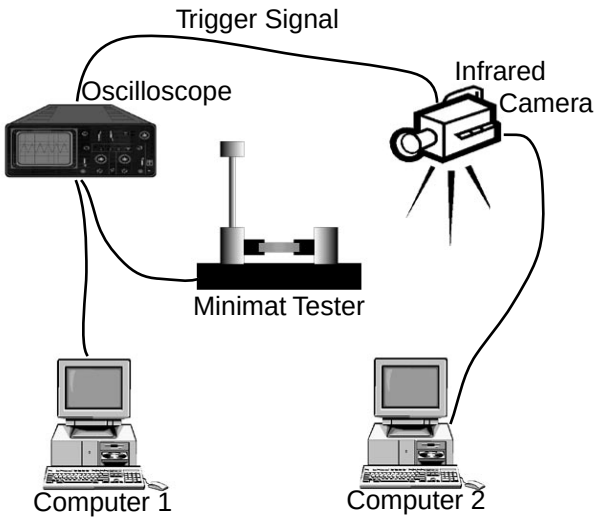

Figure 9: Schematic of the experimental setup showing the infrared imaging system, the loading device and the data acquisition system, after Wang [33].

The IR imaging system was calibrated using a Mikron M340X black body calibration source for temperatures up to 30°C above ambient temperature. The signal response of the imaging system is close to linear. Surface emissivity of the painted specimen was measured by comparison with the black body source. After calibration and 12 bit data digitization, the system permits a resolution of up to 0.01°C and an absolute accuracy up to 0.10°C.

5.3 Coupled thermal stress FEA

The experiments were simulated by 2D coupled temperature displacement analysis using ABAQUS [30], a commercially available FEA code. ABAQUS permits a fully coupled analysis by adding temperature as an additional nodal degree of freedom and solving the thermal and mechanical systems simultaneously using Newton's method. This technique permits variation of mechanical properties with temperature. However, in the current study the maximum temperature rise is below 40°C and thus the expected change in material properties, such as, the flow stress and modulus of elasticity is negligible. Conversion of plastic work to heat was modeled by extracting the stress and plastic strain fields at each increment of the nonlinear analysis, computing the plastic work and supplying a fraction, β, of this as a heat source back to the analysis at every material point. The fraction of plastic work converted to heat, β, was assumed to be a multi-step function of strain varying from a 0.45 to 0.7 based on experimentally measured data [8].

302 SS was modeled with a rate independent, isotropic hardening, Mises plasticity material model. ABAQUS [30] assumes associated flow and solves the plasticity equations numerically by applying the backward Euler method to the flow rule. Experimentally measured (Figure 8) [8] uniaxial test data was used to define the evolution of flow stress.

Coefficient of Thermal Expansion	(α)	17.3×10^{-6}	$1/^{\circ}$C
Thermal Conductivity	(k)	15.7	W/m$^{\circ}$C
Specific Heat	(c)	500	J/kg m^3
Density	(ρ)	8000	kg/m^3
Modulus of Elasticity	(E)	193	GPa
Yield Stress	(σ_y)	380	MPa

Table 1: Material properties of 302 stainless steel based on [34].

Standard tabulated [34] values were used for other mechanical and thermal properties (Table 1).

Plane stress conditions were assumed and the lower symmetric half of the specimen was modeled. A mix of 4 noded (bilinear in both displacement and temperature) and 8 noded (biquadratic in displacement and bilinear in temperature) elements were used. Characteristic element length near the crack tip is 0.05 mm. Crack propagation was modeled by node release along the crack front. Crack length history was obtained from the thermal images by using an edge detection algorithm to find the crack tip. This was supplied as input to the simulation for node debonding. A constant velocity boundary condition was applied to one end of the model to simulate the constant pulling rate used in the experiment. Constant temperature boundary conditions were imposed at one end of the sample to simulate the very large heat capacity of the clamps compared with the specimen. No heat transfer is assumed at the free edges and across the symmetry line of the model.

5.4 Results and discussion

The experimentally measured load history is compared to the computed loads in Figure 10. Simulation results predict forces that are within 10% of those recorded experimentally. Since the specimen was pulled at a constant rate, the area under the force history plot is proportional to the work done at the boundary. Thus, a good match in these curves suggests a good match in the global energy input into the specimen.

Figure 11 compares the experimentally measured temperature field with the results of the FEA. At any instant, the isotherms are concentric and move with the crack tip. This suggests that the heating is conduction dominated. The temperature field also shows a band of temperature higher than the background temperature extending from the crack tip to the free boundary suggesting active yielding in this region. This is verified by comparing with the strain rate field, $\dot{\epsilon}_{yy}$, (Figure 12) which shows a similar zone of active deformation, though less intense than that occurring in the immediate vicinity of the crack tip.

Peak temperature histories observed in the experiment are compared with simulated results in Figure 13. The finite spatial resolution of the imaging system yields temperatures averaged over a region of size 8.85×10^{-3} mm^2. Since the typical crack tip element size in the FEA was a fourth of this area, a moving spatial average (2 element x 2 element mean filter) of the FEA data was performed in order to make the comparison consistent. The temperatures predicted by FEA closely match experimental results for the first two-thirds of the test, after which the simulation predicts lower peak temperatures. This discrepancy is consistent with the thermal field data (Figure 11), where in the later stages of the test, temperatures predicted by FEA are more diffuse and less

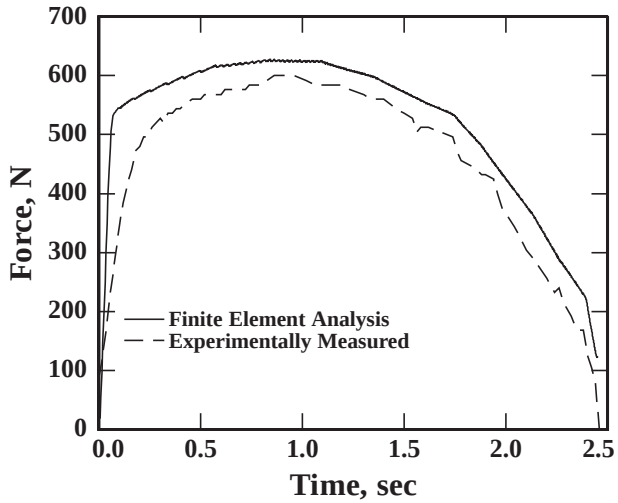

Figure 10: Comparison of measured and computed load record.

concentrated at the crack tip than in the infrared images. There is some evidence of this in the field data even at earlier times (t=1.2 sec). This is also reflected in Figure 14, which plots the instantaneous variation of temperature along the crack front. The peak temperatures from the FEA and the experiments match well but the mathematical model predicts a more gradual fall in temperatures away from the crack tip.

The net plastic dissipation can be approximated from the thermal images by integrating eq. (13) over the entire specimen. This is compared in Figure 15 with the total work, which is the sum of plastic work and recoverable elastic work; and plastic work done on the specimen computed from the FEA. The experimentally measured plastic dissipation follows the net heat content of the specimen, which goes through three phases: an initial dip in measured heat due to thermoelastic cooling, followed by a steady increase in thermal energy as work input at the specimen boundary is dissipated as plastic work near the crack tip and finally cooling due to convection, radiation and conduction through the clamps after failure. Thermoelastic cooling is clearly small and has a negligible effect on the total energy balance in later stages of the test.

Plastic dissipation computed from infrared images (Figure 15) is about 40% lower than that predicted by FEA. This discrepancy could be a result of ignoring the strain dependence of the fraction of plastic work converted to heat. Since information about the strain field was not available from experiments, a constant values of $\beta = 0.6$ has been assumed in analysis of the thermal images, eqs. (17)-(20). This was based on experiments (Zehnder, Babinsky and Palmer, [8]) that measured β for strains up to 0.15%. The FEA shows plastic strains that are much higher ($\epsilon^p_{eq} = 0.25$ to 0.5) in the region just ahead of the crack where most of the plastic dissipation takes place. As pointed out in section 2, there is experimental evidence that for very large strains, $\beta \to 1$. A higher value of β would bring computations of plastic work based on infrared images in closer agreement with simulation results.

The strain dependence of β is accounted for in the FEA. However, it is modeled as a decreasing function of strain ranging from 0.7, at low values of strain, to 0.45, for

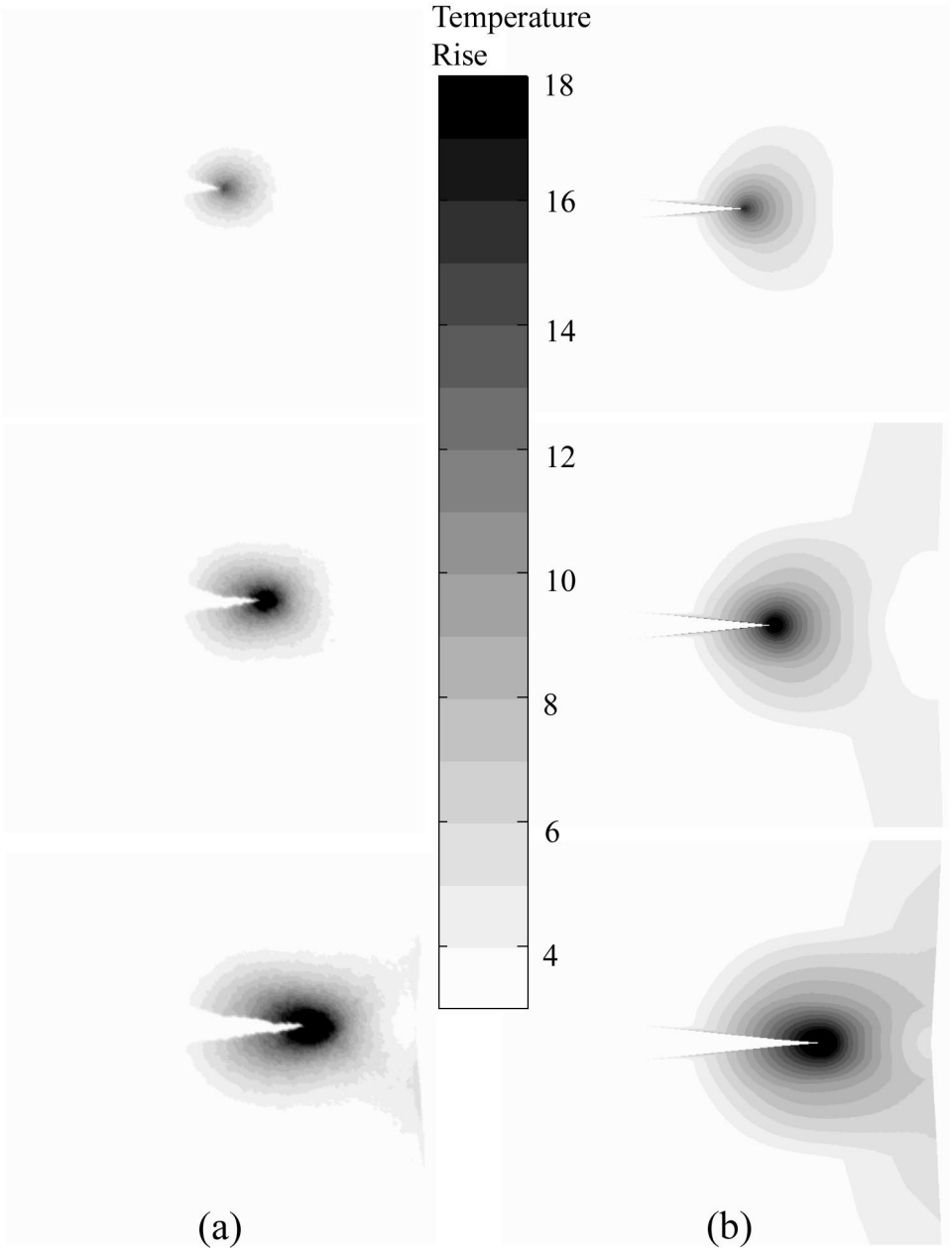

Figure 11: Comparison of infrared images (a) and temperature field computed using FEA (b). A region of size 24mm x 24mm is shown.

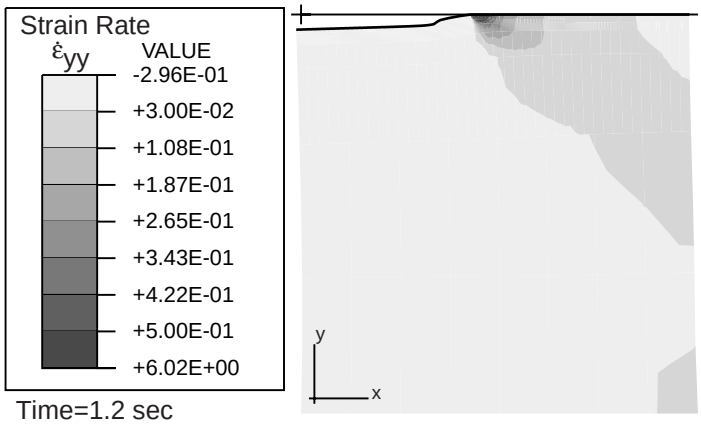

Figure 12: Instantaneous strain rate field, $\dot{\epsilon}_{yy}$, from FEA. These contours are indicative of the current active yielding zone. Lower half of the entire sample is shown.

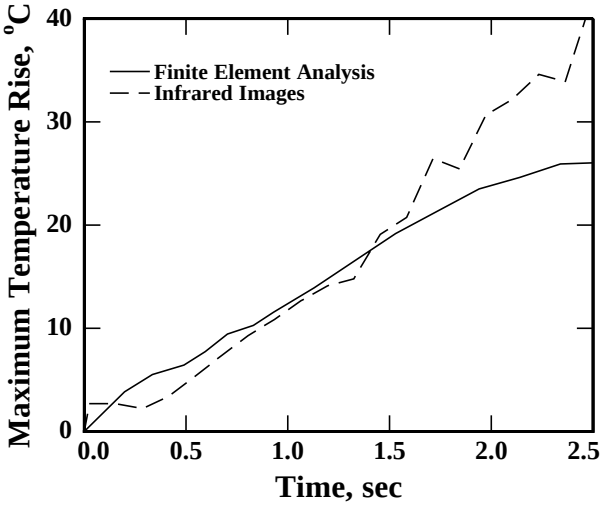

Figure 13: Peak temperature histories from FEA and infrared images. A mean filter (2 elements x 2 elements) was applied to the FEA in order to match the spatial resolution of the model to the IR camera resolution.

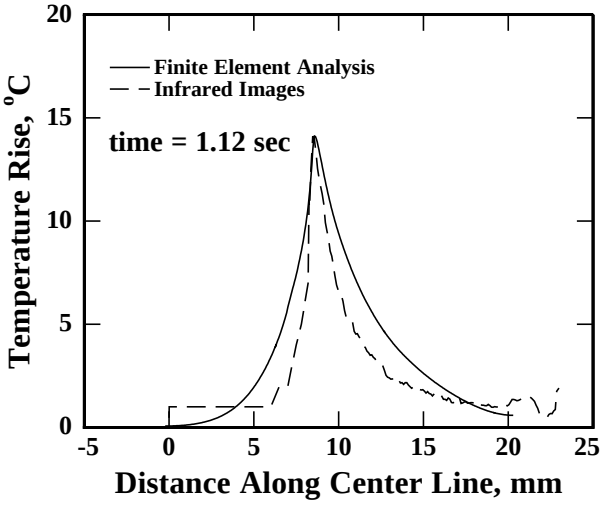

Figure 14: Temperature distribution along the crack front: Comparison of simulated and experimental results.

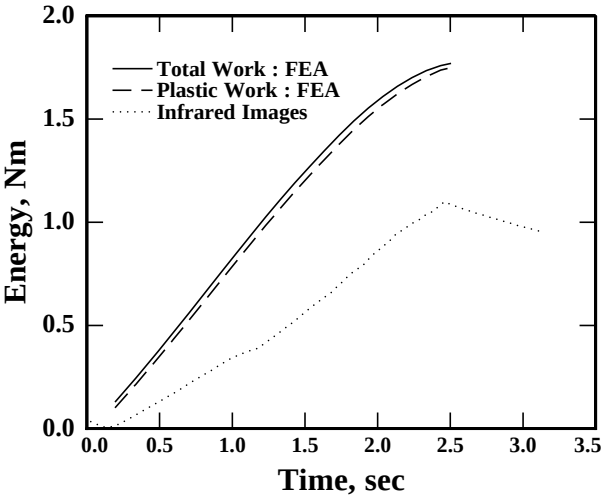

Figure 15: Total work done at the boundary of the specimen from FEA, plastic work from FEA and plastic dissipation computed from thermal images based on eq. (13).

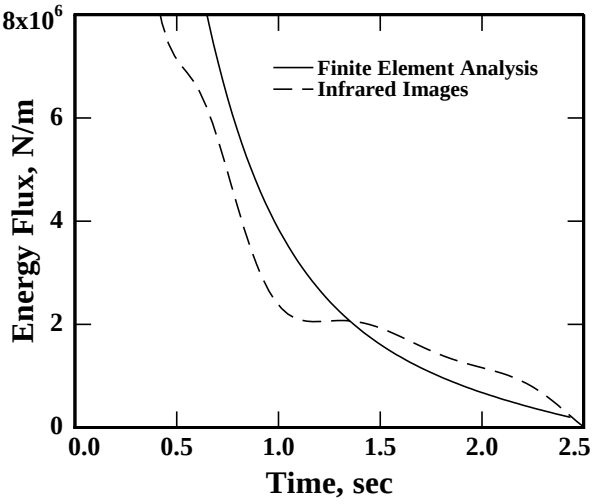

Figure 16: Energy flux, G, to the crack: Comparison of results derived from infrared images and those derived from finite element analysis.

strains above 15%. If in fact, β is much higher in the regions of high strain than used in FEA, then simulated peak temperatures would be lower than experimentally measured values and the simulated isotherms would be less concentrated at the crack tip than in the infrared images, as has been observed in Figures 11, 13 and 14.

Thus, discrepancies in the near crack tip temperature field are likely due to incomplete information about β for large strains. Away from the crack tip, where the rise in temperature is less than 5^oC, the FEA predicts slightly higher temperature than the infrared images. We suspect that this is related to the calibration of the infrared camera in the lower temperature range.

The dynamic energy release rate, G, was extracted from the thermal images using equation (18). This is plotted along with the estimate of G from FEA using equation (16) in Figure 16. The agreement between the energy flux derived from the thermal images and from the finite element analysis is very good. This contrasts with the results obtained by Zehnder and Rosakis [26] and by Kallivayalil and Zehnder [28] for dynamic crack growth. In those experiments the energy flux to the crack tip derived from the IR data was at least seven times larger than expected based on the known dynamic fracture touhgnesses of the materials. Thus, in this study we have shown for the first time that careful IR imaging of fracture can be used to derive quantitative information about energy dissipated during failure.

While there have been several experimental and theoretical analyses of the heat generated in crack propagation, systematic studies combining thermal imaging and simulations to demonstrate the consistency and accuracy of the methods are rare. The authors are unaware of any such study for processes that are not steady state or adiabatic in nature.

Dynamic crack tip temperature measurement is experimentally challenging and pushes the limits of technology. In contrast, stable crack growth can be imaged using commercially available infrared cameras. As has been shown in this study, the thermal fields in low strain rate deformation may not be strong enough to affect the mechanics of damage but they, nevertheless, carry quantitative information of the damage to the material. Qualitatively, for slow deformation rates, the temperature fields resemble the current damage zone, or the active plastic zone for running cracks. As the deformation rates are increased, conduction of heat away from the zone of distributed plasticity becomes less significant and it is expected that in such a situation the form of the imaged isotherms would resemble the accumulated damage.

Although this research effort has focused on failure of metals, the methodology has applications to distributed damage in composites as well. Thermal imaging provides quantitative information of energy dissipation during failure, which can be invaluable in the design of light weight energy absorbing structures, such as automobile bumpers.

6 Transient thermal fields in metal cutting

Material removal processes inherently involve material failure and separation. In many cases, material separation occurs along a predefined path determined by tool geometry and other cutting parameters. In a certain sense, metal cutting is a controlled failure experiment where the global nature of failure is decided apriori. Deformation and failure phenomena such as temperature rise, nature of chips formed - segmented or continuous, and friction between the tool and the chip are closely coupled and directly affect tooling costs, surface finish and process automation feasibility.

In orthogonal cutting the cutting edge of the tool is perpendicular to the direction of relative motion of the workpiece and tool as shown in Figure 17. The cut material is called the chip. The chip can be continuous, segmented (as shown) or discontinuous depending on various cutting parameters. The material undergoes deformation mainly in two regions. The first is a narrow zone ahead of the cutting tool called the primary shear zone. The second is the zone of deformation where the chip slides at high velocities and high contact pressures along the cutting tool. This zone is called the secondary shear zone.

The primary and secondary shear zones are the two regions where most of the heat in machining is generated. The mechanics of cutting is greatly influenced by this heat, as sketched in Figure 18 which outlines the complex thermo-mechanical couplings of metal cutting. This coupling affects cutting forces, chip formation, temperature fields in the workpiece, tool life and the quality of surface finish. The increased temperature in primary shear zone results in thermal softening of the material leading to reduced cutting forces. However, as cutting forces decrease, the heat dissipation decreases and thus the new material being cut no longer undergoes thermal softening. Hence cutting forces again increase. This can give rise to oscillations in cutting forces and result in the formation of chips with very high localized deformation. These regions of high deformation are called shear bands. Xie [35], Komanduri [36, 37], and Davies [38] have studied formation of shear bands in machining of various materials including nickel alloys, steel and Ti-6Al-4V. They show how for a given workpiece material, the type of chip formed changes with cutting speed.

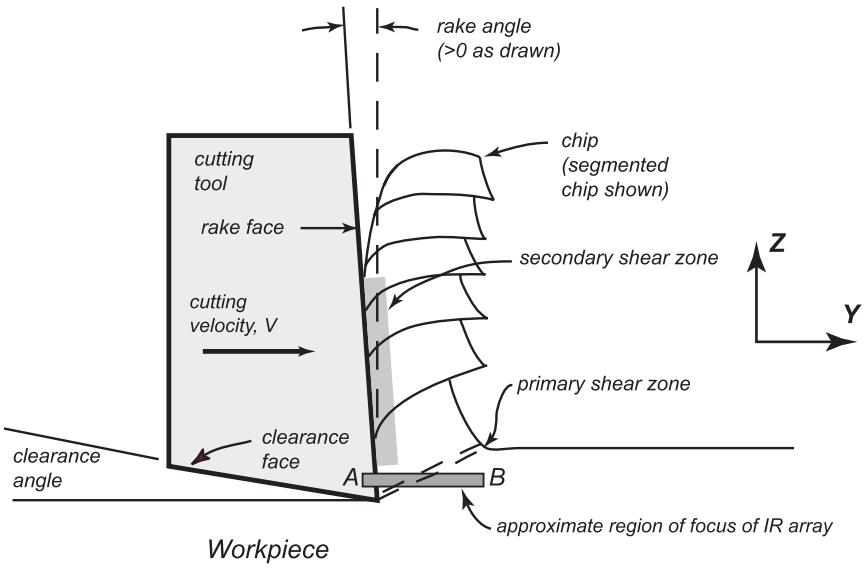

Figure 17: Geometry and terminology of orthogonal metal cutting.

6.1 Motivation for temperature measurement

We have seen that metal cutting is a complex thermo-mechanically coupled process. Its understanding is crucial in the development of machining techniques for new materials and successful commercialization of high speed machining. There exist many machining handbooks giving recommendations for various cutting parameters for specific materials which have been used for decades in the manufacturing industry. However, with the ever expanding field of engineering materials, increasing machining speeds and modern short product life cycles, the machining industry would benefit greatly from reliable and inexpensive ways to optimize machining processes.

Quantitative theoretical predictions are difficult or impossible due to the complexity of the problem and lack of reliable and realistic models for material properties, friction and heat transfer. The strong thermo-mechanical coupling has made a complete theoretical analysis unsolvable. Thus, there are substantial efforts now underway to develop computational mechanics simulations of metal cutting. In the light of current and anticipated advances in simulation, the nature of data obtained from conventional metal cutting experiments is not sufficient to validate the simulations. Most experiments are done under steady state cutting, whereas modeling capabilities generally allow simulation of only a small duration of the actual cutting process. Also, many machining methods such as milling include intermittent contact of the tool with the workpiece. To better refine the process and to validate the simulations, it is necessary to gather experimental data for such transients at the same temporal and spatial resolution as one is able to predict from modeling.

Simulations require the following inputs: 1) Geometry of cutting i.e. depth of cut, rake angle etc., 2) Material properties at high strain rates (up to 10^5/s) and high temperatures (up to 1000°C) 3) Material separation/failure criteria, 4) Friction conditions

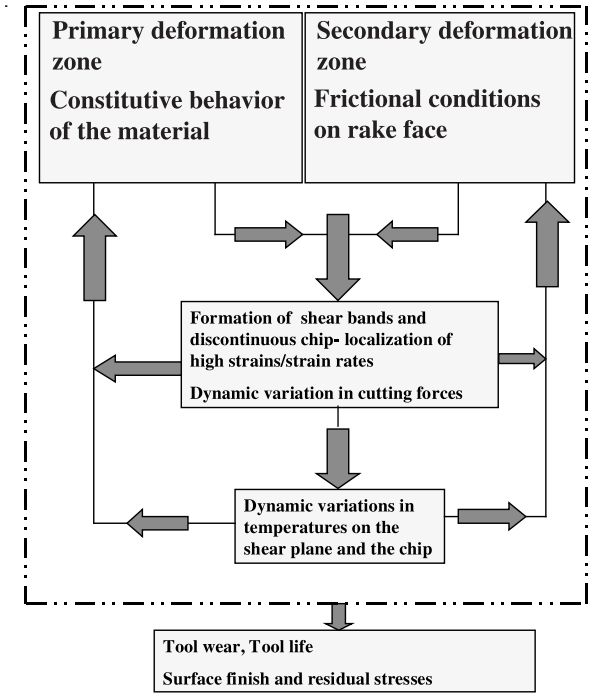

Figure 18: Illustration of thermo-mechanical coupling in metal cutting.

at tool/chip interface and 5) Fraction of plastic work dissipated as heat. The output of a simulation can contain all or some of the following information: 1) Forces, 2)Strains, strain rates, 3) Temperatures 4) Residual stresses and 5) Chip type.

We note that there is significant uncertainty associated with a number of input parameters. The conditions of machining are so unique that very little is known about material properties and frictional conditions under those situations. Hence, one must rely on intelligent guesses to start modeling. Given this, if we can measure and compare at a fine scale some of the output variables, input parameters can be refined and significant progress can be made in building robust and reliable models of machining.

With this in mind, we present in section 6.4 an experimental setup to measure temperatures in transient orthogonal metal cutting. Resolution of temperatures is obtained on time scales of 200 ns and areas as small as 27 x 27 μm. The experiments are aimed at generating data for transient cutting conditions which can be modeled by finite element simulation.

6.2 Survey of temperature measurements in machining

One of the earliest attempts to measure temperatures was reported by Boothroyd [39]. He photographed the tool, chip and workpiece using an infrared sensitive photographic plate. The optical density of the plate was calibrated against the temperature of the surface it sees during the exposure time. He conducted orthogonal machining experiments on a tube of 0.14 carbon steel, 50 mm outside diameter, 3.125 mm wall thickness. The tube

was faced on a lathe with a cutting tool slightly wider than the wall of the tube. The photographic plate was sensitive to temperatures above 500°C and for a range of about 200°C. Since the shear zone temperatures were expected to be in the range of 200-300°C, the workpiece was preheated to 350°C. The sensitivity of the photographic plate required an exposure time of 10-15 seconds. Thus the resulting photograph was an average of the temperature during the exposure period, and only steady state cutting conditions could be examined. The method was able to capture the feature that the highest temperatures occur at the tool-chip interface on the rake face, some distance from the cutting edge, which qualitatively agreed with analytical results.

Chao, et al. [40] used a lead sulphide (PbS) photoconductive cell to measure temperature distribution at the tool flank. The time constant of the photoconductive cells used was estimated to be about 100 μs or less. They machined a tubular workpiece 225mm outside diameter and 4.75mm wall thickness in a similar fashion as Boothroyd. However, they provided an axial slot in the workpiece to accommodate the PbS cell assembly. Radiant energy emitted at the tool flank was seen by the cell through 2.4mm diameter holes drilled axially in the tube wall. The region seen by the cell is controlled by the 127 μm aperture of the cell. The output of the cell was calibrated by using a heated carbide strip of identical material to that used in the cutting tool. They measured the temperatures in cutting AISI 1018 and AISI 52000 steels at speeds in the range of 1 to 2.75 m/s.

Prins [41] used a radiation pyrometer mounted above the tool to measure rake face temperatures. Again, the cutting geometry was similar to that employed by Boothroyd and by Chao et al. The workpiece material was Ck45 steel in normalized condition and tools were carbide. The cutting speed range was 1.5-3 m/s. Uniformly spaced holes of 3mm diameter were drilled in the workpiece parallel to the axis of rotation, so that chips produced have holes in them at regular intervals. This allowed the pyrometer to see the rake face of the tool intermittently as the chip flows over the rake face. The temperature of the whole contact area was measured by changing the position of the hole along the width of the chip and moving the pyrometer perpendicular to the cutting edge. The sensing element of the pyrometer was an infrared photo-transistor with peak sensitivity at a wavelength of 1.43 μm. The aperture for the transistor was 600 μm and a 3X optical system was used, thus the spot seen on the tool by the transistor was 200 μm. The time constant of the transistor was about 50 μs. He also found that the maximum temperature occurs some distance behind the cutting edge.

Lezanski and Shaw [42] measured mean cutting temperatures in milling using the tool-chip thermocouple technique. They tested the hypothesis that the tool temperatures at the end of intermittent cuts would decrease with increase in cutting speed. They conducted experiments on AISI 1018, 1045, grey cast iron, AISI 2024 aluminum and AISI 31600 bronze. They used high speed steel (HSS) and carbide cutting tools at cutting speeds up to 3 m/s for steel and grey cast iron, up to 7.5 m/s for aluminum and 5 m/s for bronze. They found that in all cases investigated, the temperature at the exit of cut did not decrease with increased speed.

Stephenson [43] reported steady state temperatures in cutting tubes in a manner similar to Boothroyd, Chao et al. and Prins. He tested 1018 steel, 2024-T4 aluminum, CA360 brass, annealed meehanite GA grey cast iron and used tungsten carbide tools. The cutting speeds were in the range of 1 to 3.9 m/s. He measured temperatures in the primary shear zone using a thermal video system. He also employed the tool-chip intrinsic thermocouple technique to measure the average temperature at the tool-chip

interface.

Ay et al. [44] measured temperatures on the tool by binding thermocouples to a carbide insert. They machined round stock of AISI 1045 on a lathe at speeds of 0.5-4 m/s

Müller-Hummel and Lahres [45,46] measured the temperature in the contact zone between chip and tool rake face by infrared thermography. They used CVD-diamond coated insert, diamond being able to transmit infrared, and drilled a hole through the bottom of the tool to create a path for infrared radiation, which was scanned by high resolution thermographic camera. They report maximum temperatures at the chip bottom as a function of cutting speeds and feeds during dry turning of AlZnMgCu1.5-malleable alloy. The testing time is 0.1 seconds for recording the temperature distribution.

Kottenstette [47] reported chip-tool interface temperature in ultra high speed machining. The experiment consisted of looking at the bottom surface of the chip by drilling a hole in the tool insert. A plastic light pipe was inserted into the hole in the insert. The radiation transmitted through the pipe was imaged on photodiode detectors. Temperature data was captured at 100 μs intervals. The pipe diameter of 1600 μm determines the region over which the temperature signal is averaged.

6.3 Analytical and computational modeling of metal cutting

The earliest models of metal cutting are attributed to Merchant [48] and Piispanen [49]. Merchant developed relations between various cutting parameters and forces required for orthogonal cutting. His theory predicts forces which are a good first approximation, however it does not account for possible changes in material properties during machining. Lee and Shaffer [50] attempted to apply plasticity theory to metal cutting assuming the material is rigid plastic. They developed a slip-line field for orthogonal metal cutting. Oxley [51] incorporated effects of strain hardening in his model. There has been some attention given to model frictional interaction between chip and tool rake face by Doyle [52]. Moufki and Molinari [53,54] have developed models accounting for the dependence of coefficient of friction on temperatures and sliding velocities.

In recent years, the finite element method has been employed with considerable success by several researchers. Strenkowski [55] employed an Eulerian formulation for steady state metal cutting simulations. Bouzid [56] used a Lagrangian formulation to predict temperature distributions. Lin [57] developed a coupled model of thermo-elastic-plastic material under large deformation and used critical value of strain energy density as separation criterion for the formation of chip. Other criteria which have been used include "distance tolerance" criterion by Komvopoulos [58], fracture mechanics based criterion by Hashemi [59] and critical stress criterion by Shet [60]. Marusich [61] successfully implemented a Lagrangian FE model with adaptive remeshing to predict segmented chip formation. Shet et al. [60] report the procedure and specific modeling techniques for simulating orthogonal metal cutting using a commercially available, general purpose finite element computer code. The finite element results presented here in section 6.5 for comparison with experimental results are from analyses carried out along the same lines as by Shet [60].

6.4 Experimental set up for temperature measurement:

The main objective of this work is to develop experimental techniques to measure temperatures on length and time scales not achieved before. We have developed a system

that can, for the first time, measure temperatures over areas as small as 27 x 27 μm and time scales of 200 ns.

Ideally in-situ temperature measurements should be performed in realistic cutting operations such as turning and milling. However, due to the extremely small field of view of the optical system and the inherent vibrations involved in any machining setup and the path of chips, one cannot be certain of the location from which the temperatures are measured. To circumvent this problem and to design an experiment tractable by FEM simulations, a transient, orthogonal cutting experiment was developed which uses a cutting tool that swings on the end of a pendulum. The details of this and subsequent results are discussed by Potdar [62]. The maximum cutting speed, limited by the length of the pendulum is about 4.5 m/s. Materials cut successfully include 1018 CR steel, 6061-T6 Al and Ti-6Al-4V at depths of cut up to 250 μm, 500 μm and 200 μm respectively. The cutting tool was a commercially available C6 grade carbide insert with 0° rake angle. The depth of cut is not constant, however for the first 3mm of cutting where we measure temperatures it changes less than 4%. The cutting force is measured via strain gauges bonded to both sides of the cutting tool holder. Rise of the force signal, indicating initial impact of the tool with workpiece provides the trigger signal to the digital oscilloscope that acquires data. To synchronize the position of the cutting tool with force and temperature signals, a photodiode circuit is used. An IR LED is placed coaxially with an IR photodiode. The cutting tool passes between them, changing the IR radiation that the photodiode receives from the IR LED. For a range of travel of about 1mm the circuit has sensitivity of approximately 2 mV for 1 μm of tool travel.

Temperature of the workpiece and the chip is measured using a linear array of 16 InSb IR detectors with 200 ns rise time. IR radiation is focused onto the detectors through a 3X reflective mirror system designed and fabricated at Cornell. The detectors are 81 μm square with 100 μm center to center spacing. Through the 3X lens, each detector focuses on a 27 x 27 μm region on the workpiece. The total field of view is 27 x 494 μm, as shown in Figure 17. The detector array was aligned parallel to the velocity of the cutting tool. Since the IR system and workpiece are securely held to an optical table, we can focus on specific locations on the workpiece with a high degree of confidence.

The optical system is focused using visible light projected through a grid. The grid is then replaced by the test specimen. The test specimen is 30mm x 20mm and 3.25mm thick. It is held in place by a specially designed rigid fixture which ensures accurate and repeatable location of the test specimen with respect to the optical system. All specimens are prepared to a uniform surface finish by fine grain sand blasting.

The tool is adjusted in the pendulum arm such that it can cut the desired depth of cut. This is achieved by using a 'set-up-specimen' which is less in height than the test specimens, the difference in heights of this specimen and the test specimens being the depth of cut. The tool is adjusted so that it is just touching the top of 'set-up-specimen. Then for the actual cutting experiment the 'set up specimen' is replaced by a test specimen.

In a single experiment, the temperatures in the region of 27 x 494 μm can be mapped. With the help of X, Y and Z translation stage on which the detectors are fixed, we can focus on any region of interest. Referring to the coordinate system shown in Figure 17, by keeping Y position fixed, we can change Z positions to see temperature evolution at various heights along the depth of cut. The accurate positioning of the detector mainly depends upon the mechanical translation stage used. With the current set up we can adjust Z position with a precision of 50 μm. Thus, in a given set of

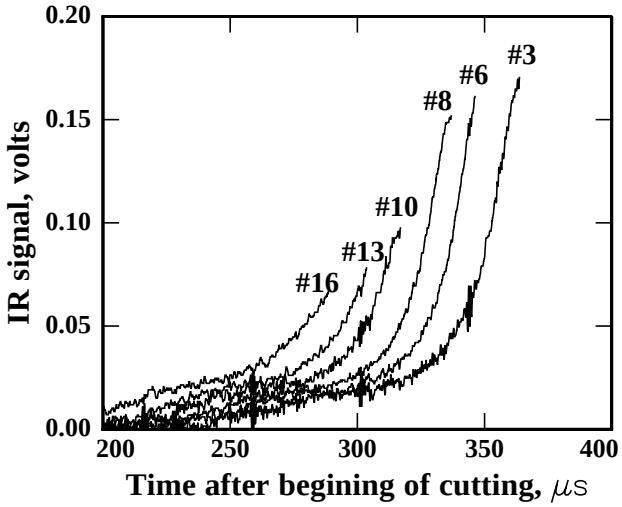

Figure 19: Experimental data (IR voltage) for cutting 1018 CRS at 4.3 m/s, 250 μm depth of cut.

experiments, we can scan all the region of interest. In some sense, each experiment is different, but we have tested the repeatability of the experiments extensively and forces, chip morphology and temperature signals for identical experiments have been found to be very repeatable.

6.5 Experimental Results

Experimental results are illustrated in Figures 19 to 23 and are compared with finite element results obtained using ABAQUS [30]. The finite element analyses used a critical stress criterion for material separation. The material model used for 1018 CR steel was adapted from Shawki and Clifton [63].

Figure 20 shows the signals from different elements of the IR array system for a single experiment cutting 1018 CR steel, at 4.3 m/s, 250 μm depth of cut. In this case, the line of view of the IR array is 250 μm above the line of cut, i.e. the view is just along the free surface of the workpiece. Detector element 16 sees the cutting first and element 3 sees the cutting last, e.g. referring to Figure 17, element 16 focuses of point A, and element 3 focuses on point B. Since this is a transient cutting experiment, we note that the temperature increases as cutting progresses. Maximum temperature at any point, such as A in Figure 17, is recorded when cutting tool is very near to A. Because of the finite resolution of any measurement system and given that highest temperatures may occur very close to tool-chip interface on length scales smaller than the resolution, experimental signals are, in some sense, lower bounds on the maximum temperatures occurring in the process. The signal on the detector drops off as the cutting tool passes through its field of view. Figure 19 shows the signal on the detector until the time instant

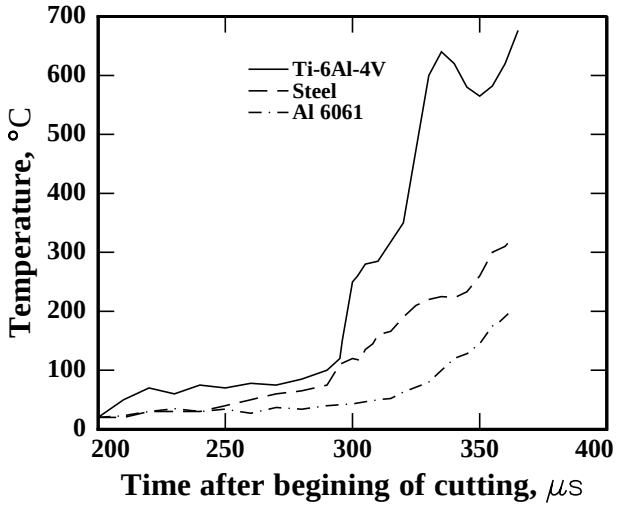

Figure 20: Evolution of temperatures at a point 1.55mm from the beginning of cutting, 250 μm above the line of cut for steel and aluminum, (250 μm depth of cut), 150 μm above the line of cut for Ti-6Al-4V (150 μm depth of cut).

at which the cutting tool passes the detector field of view.

Figure 20 shows the temperature corresponding to the signal in Figure 19 for element 3, as well as temperatures for 6061-Al and Ti-6Al-4V samples. Note that the results for the Ti-6Al-4V samples are for 150 μm depth of cut and thus the height for which temperature evolution is shown is 150 μm above the line of cut. Figure 21 shows the comparison of FE study with experiments for temperature evolution. We note that FE model is able to track temperature rise but consistently shows higher temperatures.

Figure 22 shows data from eight repeat experiments. In each experiment the IR array was translated upward by about 100 μm. The peak temperature from each experiment is recorded here. This data can be interpreted as the temperature on a path more or less parallel to the rake face. Exactly how straight and how close is this line to the rake face, is difficult to say since this data comes from eight different experiments. In this case, the peak temperature is about 320°C, 250 μm above the tool tip.

Also, from the above set of experiments temperature distribution ahead of tool tip can be illustrated. Figure 23 shows the temperature distribution ahead of cutting tool after 350 μs of cutting. The data shown in the figure is obtained from three separate experiments, in which detectors were focused on horizontal lines 50, 150 and 200 μm above the line of cut. It is compared with FE contour plot. FE temperature field agrees well at 100 μm and above the line of cut. Close to tool tip just above the line of cut the FE temperature field decreases rapidly in magnitude whereas the experimental contours show more gradual change. In general, the finite element contours are more closely packed than the measured results. Further experiments, possibly with a two-dimensional detector array would help resolve these discrepancies.

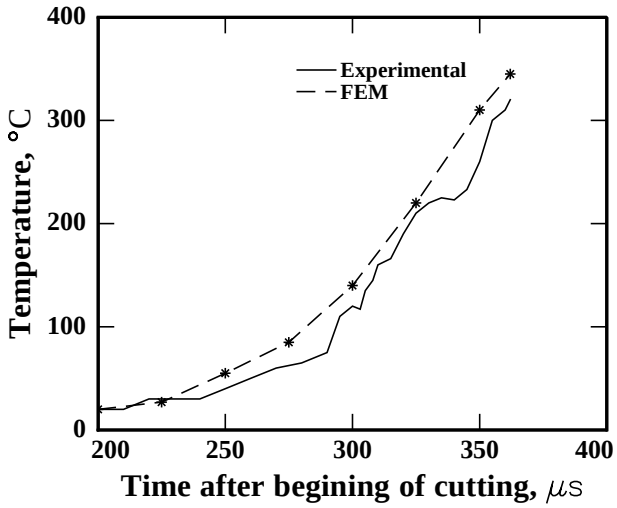

Figure 21: Comparison of experimental and FE results for evolution of temperature at a point 1.55mm from the beginning of cutting while cutting 1018 CR steel at 4.3 m/s, 250 μm depth of cut.

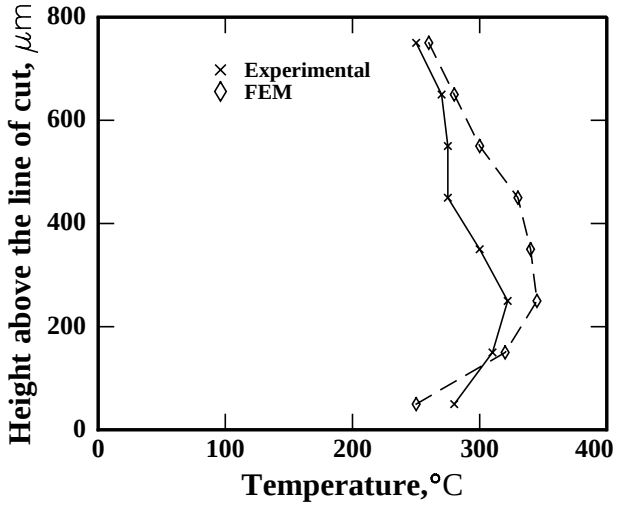

Figure 22: Maximum temperatures reached vs. height above the line of cut, while cutting 1018 CR steel at 4.3 m/s, 250 μm depth of cut.

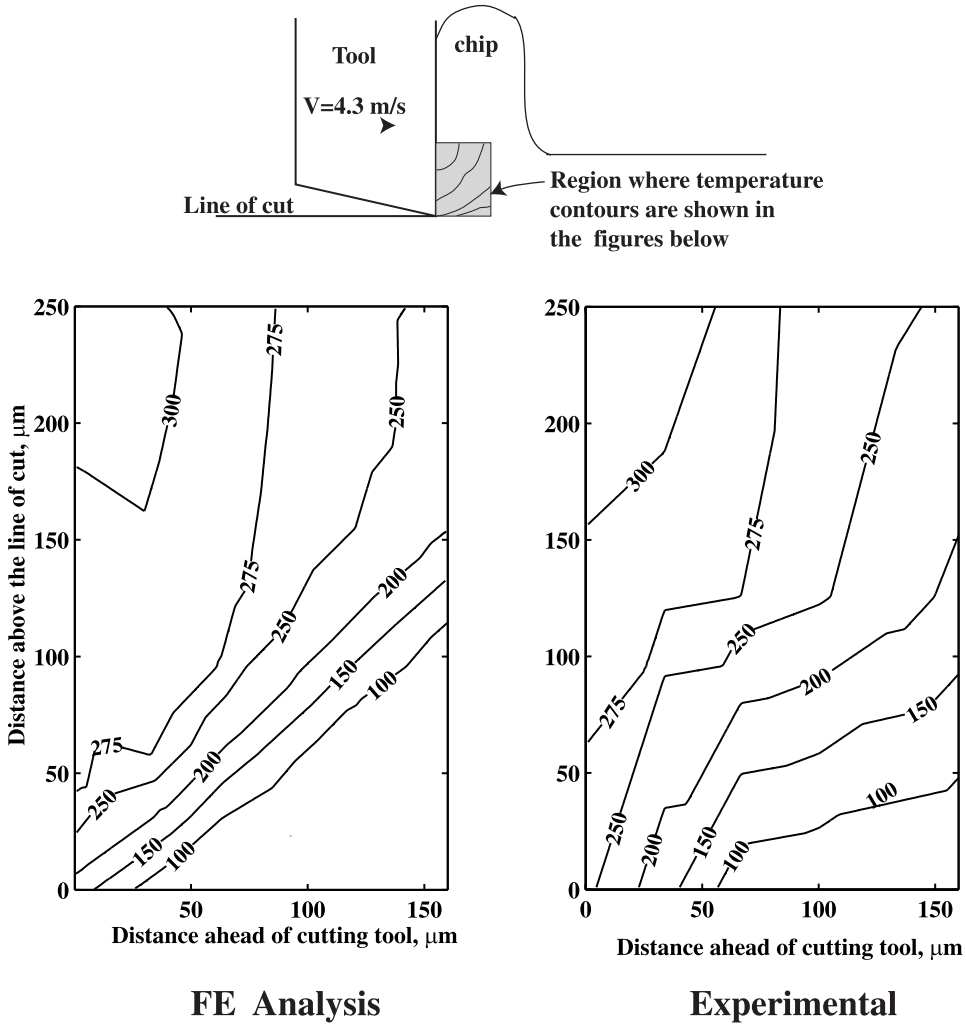

Figure 23: Comparison of finite element (FE) and experimental temperature field for cutting 1018 CRS at 4.3 m/s, 250 μm depth of cut, 350 μs after the beginning of cut.

7 Summary and conclusions

Temperature increases due to plastic work and due to friction during rapid deformation and failure processes can play an important role in the outcome of the process and can be used to probe the process itself. For most metals experimental results show that the fraction of plastic work dissipated thermally is close to one for very large strains. For smaller strains this fraction may either increase or decrease with strain. Results show that the fraction may be as low as 40% for small strains. During dynamic crack growth, plasticity induced heating can raise crack tip temperatures to as much as 400°C or more. Thermo-mechanical analysis of dynamic crack growth with such large temperature increases shows that the crack tip temperature can increase dynamic fracture toughness by delaying the onset of ductile to brittle transition. During stable crack growth, the peak temperature may not be so large, but the temperature field can be used to quantitatively extract energy dissipation due to fracture. It is anticipated that a similar approach could be used to quantify local energy absorption in complex structures. The large temperature increases that occur during metal cutting play an important role in tool life, chip formation and cutting forces. We have shown that using high speed IR detectors we can make high speed, high resolution measurements of temperature field during transient cutting. The spatial resolution of 27 μm and time resolution of 200 ns are much better than has been achieved by previous researchers. The resulting temperature field details can be used to help develop metal cutting simulations.

Acknowledgements

The metal cutting portions of this work were performed with support from the National Science Foundation (CMS-9700698). This work made use of the Cornell Center for Materials Research Shared Experimental Facilities, supported through the National Science Foundation Materials Research Science and Engineering Centers Program (DMR-0079992). The first author wishes to thank Professors Robert Thomas and Lawrence (Skip) Favro of Wayne State University for hosting him for a week in 1996 during which the thermal images of section 5 were obtained.

References

[1] Bell, J., *The Experimental Foundations of Solid Mechanics,* Springer-Verlag, Berlin and New York, 1973.

[2] Farren, W.S., and Taylor, G.I., The heat developed during plastic extension of metals, *Proceedings of the Royal Society, Series A,* **107**, pp. 422-451, 1925.

[3] Taylor, G.I., and Quinney, M.A., The latent heat remaining in a metal after cold work, *Proceedings of the Royal Society, Series A,* **143**, pp. 307-326, 1934.

[4] Bever, M.B., Holt, D.L., and Titchener, A.L., The stored energy of cold work, *Progress in Materials Science,* **17,** 1973.

[5] Maugin, G.A., *The Thermomechanics of Plasticity and Fracture,* Cambridge University Press, 1992.

[6] Carlson, D.E., Linear thermoelasticity, in *Encyclopedia of Physics, Volume VIa/2, Mechanics of Solids II,* ed. C. Truesdell, Spring-Verlag, Berlin and New York, pp. 297-345, 1972.

[7] Hodowany, J., Ravichandran, G., Rosakis, A.J., and Rosakis, P., Partition of plastic work into heat and stored energy in metals, *Experimental Mechanics,* **40**, pp. 113-123, 2000.

[8] Zehnder, A.T., Babinsky, E., and Palmer, T., Hybrid method for determining the fraction of plastic work converted to heat, *Experimental Mechanics,* **38**, pp. 295-302, 1998.

[9] Williams, R.O., The stored energy of copper deformed at 24°C, *Acta Metallurgica,* **13**, pp. 163-168, 1965.

[10] Mason, J.J., Rosakis, A.J., and Ravichandran, G., On the strain and strain rate dependence of the fraction of plastic work converted to heat: an experimental study using high speed infrared detectors and Kolsky bar, *Mechanics of Materials,* **17**, pp. 135-145, 1994.

[11] Wolfenden, A., Energy stored in polycrystalline copper deformed at room temperature, *Acta Metallurgica,* **19**, pp. 1373-1377, 1971.

[12] MacDougall, D., Determination of the plastic work converted to heat using radiometry, *Experimental Mechanics,* **40**, pp. 298-306, 2000.

[13] Kapoor, R., and Nemat-Nasser, S., Determination of temperature rise during high strain rate deformation, *Mechanics of Materials,* **27**, 1-12, 1998.

[14] Nabarro, F.R.N., *Theory of Crystal Dislocations,* Dover Publications, New York, pp. 691-694, 1987.

[15] Zehnder, A.T., A model for the heating due to plastic work, *Mechanics Research Communications,* **18**, pp. 23-28, 1991.

[16] Aravas, N., Kim, K.S., and Leckie, F.A., On the calculations of the stored energy of cold work, *Journal of Engineering Materials and Technology,* **112**, pp. 465-475, 1990.

[17] Rosakis, P., Rosakis, A.J., Ravichandran, G., and Hodowany, J., A thermodynamic internal variable model for the partition of plastic work into heat and stored energy in metals, *Journal of the Mechanics and Physics of Solids,* **48**, pp. 581-607, 2000.

[18] Rice, J.R., and Levy, N., Local heating by plastic deformation at a crack tip, in *Physics of Strength and Plasticity,*, ed. A.S. Argon, MIT Press, Chapter 20, pp. 277-293, 1969.

[19] Carslaw, H.S., and Jaeger, J.C., *Conduction of Heat in Solids,* Clarendon Press, Chapter 14, pp. 353-365, 1986.

[20] Weichert, R., and Schönert, K., Heat generation at the tip of a moving crack, *Journal of Mechanics and Physics of Solids,* **26**, pp. 151-161, 1978.

[21] Weichert, R., and Schönert, K., On the temperature rise at the tip of a fast running crack, *Journal of Mechanics and Physics of Solids,* **22**, pp. 127-133, 1978.

[22] Kuang, Z-B., and Atluri, S.N., Temperature field due to a moving heat source: a moving mesh finite element analysis, *Journal of Applied Mechanics,* **52**, pp. 274-280, 1985.

[23] Bui, H.D., Ehrlacher, A., and Nguyen, Q.S., Thermomechanical coupling in fracture mechanics, in *Thermomechanical Couplings in Solids,*, ed. H.D. Bui and Q.S. Nguyen, Elsevier Science Publishers, pp. 327-341, 1987.

[24] Malali, P.N., *Thermal Fields Generated by Dynamic Mode III Fracture in Ductile Materials*, Masters Thesis, The Johns Hopkins University, 1988.

[25] Li, W., Deng, X., and Rosakis, A.J., Determination of temperature field around a rapidly moving crack-tip in an elastic-plastic solid, *International Journal of Heat and Mass Transfer,* **39**, pp. 677-690, 1996.

[26] Zehnder, A.T., and Rosakis, A.J., On the temperature distribution in the vicinity of dynamically propagating cracks in 4340 steel, *Journal of the Mechanics and Physics of Solids,* **39**, pp. 385-415, 1991.

[27] Zehnder, A.T., and Rosakis, A.J., Temperature rise at the tip of dynamically propagating cracks: measurements using high speed infrared detectors," in *Experimental Techniques in Fracture, III,* ed. J. Epstein, VCH Publishers, pp. 125-170, 1993.

[28] Kallivayalil, J.A., and Zehnder, A.T., Measurement of the temperature field induced by dynamic crack growth in Beta-C titanium, *International Journal of Fracture,* **66**, pp. 99-120, 1994.

[29] Kallivayalil, J.A., Hui, C.-Y., and Zehnder, A.T., A method for thermo-mechanical analysis of steady state dynamic crack growth, *International Journal of Solids and Structures,* **33**, pp. 1867-1889, 1996.

[30] Hibbitt, Karlsson and Sorenson, Inc., Providence, RI, *ABAQUS User's Manual,* Version 5.8, 1996.

[31] Moran, B., and Shih, C.F., Crack tip and associated domain integrals from momentum and energy balance, *Engineering Fracture Mechanics,* **27**, pp. 615-642, 1987.

[32] Freund, L.B., *Dynamic Fracture Mechanics,* Cambridge University Press, 1990.

[33] Wang, Y., *Study of Deformation and Fracture of Polymers and Metals Using Infrared Imaging Methods*, Ph.D. Thesis, Wayne State University, 1997.

[34] Boyer, H., editor, *ASM Metals Handbook,* American Society for Metals, 1985.

[35] Xie, J.Q., Bayoumi, A.E., and Zbib, H.M., A study on shear banding in chip formation of orthogonal machining, *International Journal of Machine Tools and Manufacturing*, **36**, pp. 835-847, 1996.

[36] Komanduri, R., Schroeder T., Hazra, J, von Turkovich, B.F., and Flom D.G., On the catastrophic shear instability in high speed machining of AISI 4340 steel, *Journal of Engineering for Industry*, **104**, pp. 121-131, 1982.

[37] Komanduri R., and Brown, R.H., On the mechanics of chip segmentation in machining, *Journal of Engineering for Industry*, **103**, pp. 33-51, 1981.

[38] Davies, M.A., Chou, Y., and Evans, C.J., On chip morphology, tool wear and cutting mechanics in finish hard turning, *Annals of the C.I.R.P.,* **45**, pp. 77-82, 1996.

[39] Boothroyd, G., Photographic technique for the determination of metal cutting temperatures, *British Journal of Applied Physics,* **12**, pp. 238-242, 1961.

[40] Chao, B.T., Li, H.L., and Trigger K.J., An experimental investigation of temperature distribution at tool-flank surface, *Transactions of the ASME ,* pp. 496-504, 1961.

[41] Prins, O.D., The influence of wear on the temperature distribution at the rake face, *Annals of the C.I.R.P.,***XVIV**, pp. 579-584, 1971.

[42] Lezanski, P., and Shaw, M.C., Tool face temperatures in high speed milling, *Journal of Engineering for Industry,* **112**, pp. 132-135, 1990.

[43] Stephenson, D.A., Assessment of steady-state metal cutting temperature models based on simultaneous infrared and thermocouple data, *Journal of Engineering for Industry,* **113**, pp. 121-128, 1991.

[44] Ay, H., Yang, W-J.,and Yang, J.A., Dynamics of cutting tool temperatures during cutting process, *Experimental Heat Transfer,* **7**, pp. 203-216, 1994.

[45] Müller-Hummel, P., and Lahres, M., Quantitative measurement of temperatures on diamond-coated tools during machining, *Diamond and Related Materials ,* **4**, pp. 1216-1221, 1995.

[46] Müller-Hummel, P., Lahres, M., Mehlhose, J., and Lang, G., Measurement of temperature in diamond coated tools during machining processes, *Diamond Films and Technology ,* **7**, pp. 219-239, 1997.

[47] Kottenstette, J.P., Measuring tool-chip interface temperatures, *Journal of Engineering for Industry,* **108**, pp. 101-104, 1986.

[48] Merchant, M.E., Mechanics of metal cutting process, *Journal of Applied Physics*, **16**, pp. 267-318, 1945.

[49] Piispanen, Theory of formation of metal chips, *Journal of Applied Physics*, **19**, pp. 876-881, 1948.

[50] Lee, E.H., and Shaffer, B.W., The theory of plasticity applied to a problem of machining, *Journal of Applied Mechanics*, **18**, pp. 405-413, 1951.

[51] Oxley, P.L.B., Humphreys, A.G., and Larizadeh, A., The influence of rate of strain hardening in machining, *Proceedings of Institute of Mechanical Engineers*, **175**, pp. 881-891, 1961.

[52] Doyle, E.D., Horne, J.G., and Tabor, D., Frictional interactions between chip and rake face in continuous chip formation, *Proceedings of Royal Society of London*, **A 366**, pp. 173-183, 1979.

[53] Moufki, A., Molinari, A., and Dudzinski, D., Modeling of orthogonal cutting with a temperature dependent friction law, *Journal of Mechanics and the Physics of Solids,* **46**, pp. 2103-2138, 1998.

[54] Molinari, A., Estrin, Y., and Mercier, S., Dependence of the coefficient of friction on the sliding conditions on high velocity range, *Journal of Tribology,* **121**, pp. 35-41, 1999.

[55] Strenkowski, J.S., and Moon, K-J., Finite element prediction of chip geometry and tool/workpiece temperature distributions in orthogonal metal cutting, *Journal of Engineering for Industry,* **112**, pp. 313-318, 1990.

[56] Bouzid, W., and Lebrun, J.L., A numerical method to determine temperature distribution in orthogonal machining, in *Numerical Methods in Industrial Forming Processes,* ed.J.-L. Chenot, R.D.Wood and O.C. Zienkiewicz, pp. 895-900, 1992.

[57] Lin, Z.C, and Lin, S.Y., A coupled finite element model of thermo-elastic large deformation for orthogonal cutting, *Journal of Engineering Materials and Technology*, **114**, 218-226, 1992.

[58] Komvopoulos, K., Erpenbeck, Finite element modeling of orthogonal metal cutting, *Journal of Engineering for Industry*, **113**, pp. 253-267, 1991

[59] Hashemi, J., Tseng, A.A., and Chou, P.C., Finite element simulation of segmented chip formation in high speed machining, *Journal of Materials Engineering and Performance*, **3**, pp. 712-721, 1994.

[60] Shet, C., and Deng, X., Finite element analysis of the orthogonal metal cutting process, *Journal of Materials Processing Technology*, **4548**, pp. 1-15, 2000.

[61] Marusich, T.D., and Ortiz, M., Modeling and simulation of high speed machining, *International Journal of Numerical Methods in Engineering,* **38**, pp. 3675-3694, 1995.

[62] Potdar, Y.K., *Ph.D. Thesis, Cornell University*, 2001.

[63] Shawki, T.G., and Clifton, R.J., Shear band formation in thermal viscoplastic materials, *Mechanics of Materials,* **8**, pp. 13-43, 1989.